Available online at www.sciencedirect.com
ScienceDirect
Journal of Computational Physics 226 (2007) 798–817
JOURNAL OF COMPUTATIONAL PHYSICS
www.elsevier.com/locate/jcp

Closed form FDTD-compatible Green's function based on combinatorics

Nimrod Rospsha, Raphael Kastner *

School of Electrical Engineering, Tel Aviv University, Tel Aviv 69978, Israel

Received 7 April 2006; received in revised form 21 November 2006; accepted 1 May 2007
Available online 31 May 2007

Abstract

The advantages of the finite-difference-time-domain (FDTD) method are often hampered by the need to model large "white spaces" between and around scattering objects. In the continuous realm, these large spaces are customarily bridged by the usage of integral operators that transform the sources to any observation point using an appropriate Green's function. A companion procedure for the discretized world can be realized in principle by straightforward sampling of the continuous Green's function. However, such a procedure does not track the FDTD algorithm and hence yields different results. Alternatively, an FDTD-compatible discrete Green's function is derived in this work with the Yee-discretized Maxwell's equations as first principles. The derivation involves a process of counting many combinations of paths in the spatial–temporal grid leading to recursive combinatorial expressions that are solved in closed form. Numerical implementations of the resultant Green's function in short-pulse propagation problems produce results validated by conventional FDTD computations. The advantages of efficient computations over large distances, in particular with regard to short pulses, are thus demonstrated.

1. Introduction

The finite-difference-time-domain (FDTD) method is a popular discretization scheme for the time-domain Maxwell's equations in their differential form. It has been used extensively to model a variety of electromagnetic problems, such as radiation, scattering and high speed circuits. The method employs central difference approximations for the derivatives sampled over the Yee grid [1,2] that ensure second order accuracy and an explicit formulation, amenable to marching-on-in-time, leapfrog type of solver. Like most differential methods, it is very compact in terms of memory allocation and computational time, having a $\mathcal{O}(N)$ computational complexity for each timestep, where N is the number of field samples within the computational domain. As is well known, this domain is bounded by absorbing boundary conditions (ABCs) of either the local or the global type. For any given computer configuration, the size of the computational domain and the temporal span

* Corresponding author. Tel.: +972 3 6407447; fax: +972 3 06423508.
E-mail address: kast@eng.tau.ac.il (R. Kastner).

0021-9991/$ - see front matter © 2007 Elsevier Inc. All rights reserved.
doi:10.1016/j.jcp.2007.05.017

will eventually be limited by the available computer resources due to the need to execute the FDTD for each one of the N points at each time step. Another well known issue [2] is dispersion, including band-stop frequencies, anisotropy and stability, associated with FDTD solution. Therefore, these solutions will not be equal, in general, to companion solutions obtained via continuous Kirchoff-type integrals (e.g., [16]). In the case of the FDTD, certain applications such as multi-body problems or evaluations of the field in constrained regions only, the mathematical operations are performed also within a large "white space" outside the regions of interest. By bridging over these regions with Kirchoff-type integrations, the advantages of the FDTD can be significantly enhanced. Additional emerging applications [4–7] now call for a fusion of the FDTD and integral operators. In these applications, discretization schemes are sometimes applied to the integral operators that contain the continuous form of the Green's functions and are not compatible with the FDTD scheme. A perfect match with unbounded FDTD computations can never be achieved in this way. Therefore, in both types of applications, the need has arisen to produce FDTD-compatible discrete formulations to the integral operators as well. The essence of these formulations is the generation of a Discrete Green's Function (DGF).

One way to obtain the impulse response is via an inverse transform of the $\mathcal{Z}$-domain [8] version, as done in [9]. A time domain DGF has been presented in [10,11] as a series of infinite products of Jacobi polynomials, whose relation to the expression below still calls further investigation. Initial work in the time domain has been recently presented in [12]. The DGF, derived therein, serves for characterizing the external domain in the context of efficient global boundary conditions. In [12], and subsequently in [13,14], the evaluation of the DGF has been done in a straightforward numerical fashion, augmented with some experimental formulas.

In this work, a systematic discrete time domain derivation of the DGF is presented. The starting point is the Yee-discretized version of Maxwell's system of equations, seen as a linear and time-invariant discrete state-space system, whose inputs and outputs are the (electric and magnetic) current density sources and the (electric and magnetic) fields, respectively, and whose impulse response is the DGF. The two cases aperture and free space source problems are defined in Section 2. The Yee-discretized Maxwell's equations are represented in graph form in the spatial–temporal space as described in Section 2. The two problems are cast in terms of path counts within the graph, and solved in closed form via combinatorial considerations. The aperture problem involves modifications of the Catalan triangle [15], while the free space source problem makes use of modifications of the Pascal triangle, as described in Sections 3.1 and 3.2, respectively. The closed form solution for the DGF is expressed as an inherently finite series in powers of the $-\gamma^2$, γ being the Courant number. Further development, designed to truncate the spatial domain in order to accommodate arbitrary boundary conditions, is described in Section 4. The results can be verified by comparison to the frequency domain, multi-dimensional inverse $\mathcal{Z}$-transform presented in [9], and the direct numerical evaluation for the the special case in [12–14]. Further verification is done in Section 5, where numerical simulations are shown for a one-dimensional pulse propagation. The DGF solution is seen to coincide with the conventional FDTD computation. The capability of using the Green's function approach in the context of the FDTD is thus validated, as summarized in Section 6.

2. Graph representation of the FDTD method

Continuous domain Green's functions such as $\underline{\underline{\mathbf{G}}}_e(\mathbf{r},\mathbf{r}';t-t')$ are used as kernels in Kirchoff-like integrations of electric ($\mathbf{J}(\mathbf{r}',t')$) and magnetic ($\mathbf{J}_m(\mathbf{r}',t')$) current sources to obtain the observed electric field $\mathbf{E}(\mathbf{r},t)$ within a volume Γ, enclosed by a closed surface $\partial\Gamma$ [16, Section 1.1]:

$$\begin{aligned}\mathbf{E}(\mathbf{r},t) = {} & \mu\frac{\partial}{\partial t}\oiint\int_{\partial\Gamma,t'}\mathbf{J}_s^{\mathrm{eq}}(\mathbf{r}',t')\cdot\underline{\underline{\mathbf{G}}}_e(\mathbf{r},\mathbf{r}';t-t')\mathrm{d}S'\,\mathrm{d}t' + \oiint\int_{\partial\Gamma,t'}\mathbf{J}_{ms}^{\mathrm{eq}}\cdot\nabla'\times\underline{\underline{\mathbf{G}}}_e(\mathbf{r},\mathbf{r}';t-t')\mathrm{d}S'\,\mathrm{d}t' \\ & + \mu\frac{\partial}{\partial t}\int\int\int\int_{\Gamma,t'}\mathbf{J}(\mathbf{r}',t')\cdot\underline{\underline{\mathbf{G}}}_e(\mathbf{r},\mathbf{r}';t-t')\mathrm{d}V'\,\mathrm{d}t' + \int\int\int\int_{\Gamma,t'}\mathbf{J}_m(\mathbf{r}',t')\cdot\nabla'\times\underline{\underline{\mathbf{G}}}_e(\mathbf{r},\mathbf{r}';t-t')\mathrm{d}V'\,\mathrm{d}t'\end{aligned} \tag{1}$$

where $\mathbf{J}_s^{\mathrm{eq}}(\mathbf{r}'\in\partial\Gamma,t') = \hat{\mathbf{n}}\times\mathbf{H}(\mathbf{r}',t')|_{\partial\Gamma}$ and $\mathbf{J}_{ms}^{\mathrm{eq}}(\mathbf{r}'\in\partial\Gamma,t') = -\hat{\mathbf{n}}\times\mathbf{E}(\mathbf{r}',t')|_{\partial\Gamma}$ in Eq. (1) are the equivalent surface sources defined over $\partial\Gamma$. Note that the region Γ need not necessarily be free space. Reducing Eq. (1) to the

one-dimensional z-dependent case, and consider separately the contributions of the surface and volume sources, as shown in Eqs. (2a) and (2b), respectively:

$$E_x(z,t) = \mu\frac{\partial}{\partial t}\int_{t'}\left[J_{sx}^{\mathrm{eq}}(z_\alpha,t')G_e(z-z_\alpha;t-t') + J_{sx}^{\mathrm{eq}}(z_\beta,t')G_e(z-z_\beta;t-t')\right]\mathrm{d}t' + \int_{t'}\left[J_{msy}^{\mathrm{eq}}(z_\alpha,t')\frac{\partial G_e(z-z_\alpha;t-t')}{\partial z'} + J_{msy}^{\mathrm{eq}}(z_\beta,t')\frac{\partial G_e(z-z_\beta;t-t')}{\partial z'}\right]\mathrm{d}t'; \tag{2a}$$

or

$$E_x(z,t) = \mu\frac{\partial}{\partial t}\int\int_{z'=z_\alpha,t'}^{z'=z_\beta} J(z',t')G_e(z-z';t-t')\mathrm{d}z'\,\mathrm{d}t' + \int\int_{z'=z_\alpha,t';}^{z'=z_\beta} J_m(z',t')\frac{\partial G_e(z-z_\beta;t-t')}{\partial z'}\mathrm{d}z'\,\mathrm{d}t' \tag{2b}$$

where the planes $\partial\Gamma_\alpha$ at $z=z_\alpha$ and $\partial\Gamma_\beta$ at $z=z_\beta$ form the closed surface bounding the computational domain γ on the left and right sides, respectively as seen in Fig. 1. Also, $J_{sx}^{\mathrm{eq}}(z_\alpha,t') = -H_y(z_\alpha,t')$, $J_{sx}^{\mathrm{eq}}(z_\beta,t') = H_y(z_\beta,t')$, $J_{msy}^{\mathrm{eq}}(z_\alpha,t') = E_x(z_\alpha,t')$, $J_{msy}^{\mathrm{eq}}(z_\beta,t') = -E_x(z_\beta,t')$, and the polarization has been set without loss of generality. Henceforth, we refer to the cases of Eqs. (2a) and (2b) as aperture and free space source problems, to be treated individually in Sections 3.1 and 3.2, respectively.

It is our goal to obtain an FDTD-compatible companion to both cases of Eq. (2). The integrations in both aperture and free space cases involve the usage of a DGF as the discrete counterpart of either G_e or $\frac{\partial G_e}{\partial z}$. For the reasons stated in Section 1, we start with the Yee-discretized Maxwell's equations, as first principles, rather then discretizing Eq. (2) directly. For a homogeneous and lossless medium, these equations are as follows:

$$\frac{\partial E_x}{\partial t} = -\frac{1}{\varepsilon}\frac{\partial H_y}{\partial z} - \frac{1}{\varepsilon}J_x \Rightarrow E_x|_k^{n+1} = E_x|_k^n - \gamma\left(H_y|_{k+\frac{1}{2}}^{n+\frac{1}{2}} - H_y|_{k-\frac{1}{2}}^{n+\frac{1}{2}} + \Delta z J_x|_k^{n+\frac{1}{2}}\right) \tag{3a}$$

$$\frac{\partial H_y}{\partial t} = -\frac{1}{\mu}\frac{\partial E_x}{\partial z} - \frac{1}{\mu}J_{my} \Rightarrow H_y|_{k+\frac{1}{2}}^{n+\frac{1}{2}} = H_y|_{k+\frac{1}{2}}^{n-\frac{1}{2}} - \gamma\left(E_x|_{k+1}^n - E_x|_k^n + \frac{\Delta z}{\eta}J_{my}|_{k+\frac{1}{2}}^n\right) \tag{3b}$$

where $z=k\Delta z$, $t=n\Delta t$, $\eta=\sqrt{\frac{\mu}{\varepsilon}}$, and $\gamma = c\frac{\Delta t}{\Delta z}$ is the Courant coefficient, and normalization of the E-field $\sqrt{\frac{\varepsilon}{\mu}}E \to E$, is also introduced. The source terms in Eq. (3) constitute either the equivalent or actual sources appearing in the models of Eqs. (2a) and (2b), respectively, making Eq. (3) applicable to both models. We now transfer Eq. (3) (without the source terms) to a graph representation as shown in Fig. 2. Detail A in Fig. 2 embodies Eq. (3a). In this Detail, $E_x|_k^{n+1}$ is defined at an "observation point", being connected via directed segments to $H_y|_{k-\frac{1}{2}}^{n-\frac{1}{2}}$, $E_x|_k^n$ and $H_y|_{k-\frac{1}{2}}^{n+\frac{1}{2}}$ that are located at their respective "initial points" adjacent to the observation point, with the weights marked on the segments. Detail B serves a similar purpose for Eq. (3b). Each of the initial points serves in turn as an observation point for other three initial points in the same manner.

Consider the spatial–temporal (k–n) FDTD grid in Fig. 3. Assume that a pulsed field is given at the initial point A. The pulse is then propagated through the grid over paths formed by causal cascades of segments, and the information collected at arbitrary observation points such as B. All causal paths are contained within the rhombus shown, and the complementary areas are defined as "dead zones". Each of the paths contributes a

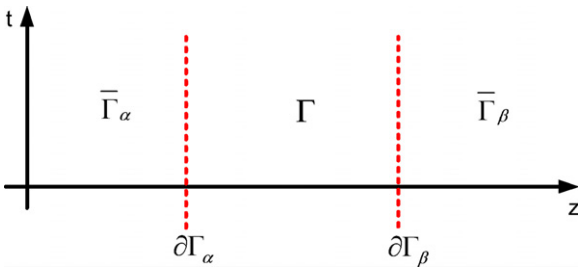

Fig. 1. One-dimensional spatial–temporal space.

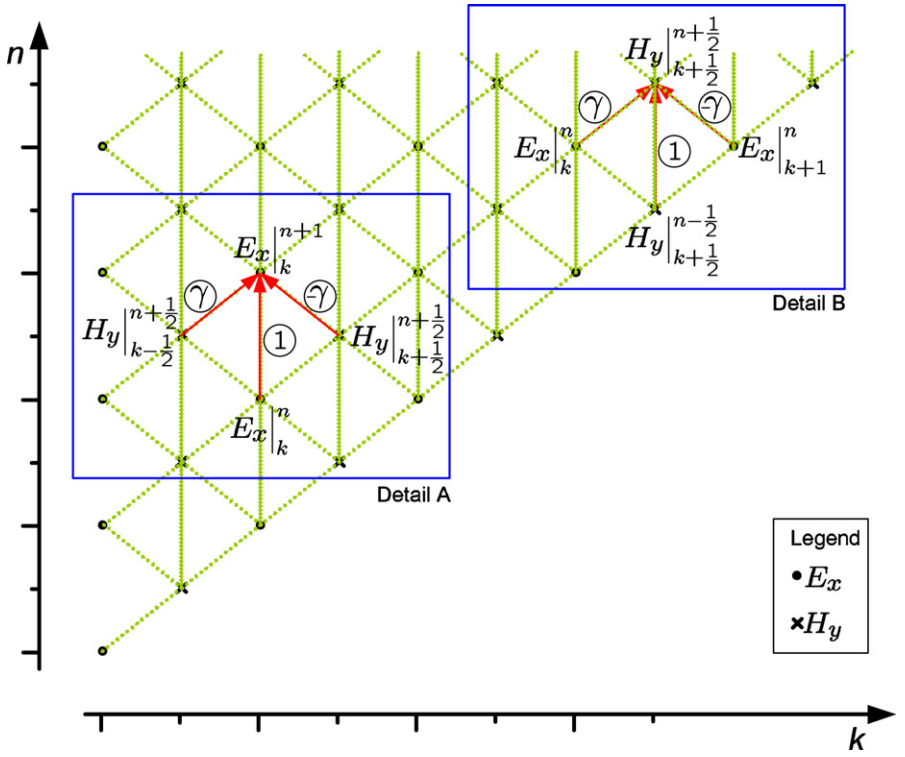

Fig. 2. Graph representations of Eqs. (3a) (Detail A) and (3b) (Detail B).

power of $-\gamma^2$ generated from the product of different upward-left directed, upward-right directed and vertically directed segments, i.e., of $-\gamma$, γ and 1, respectively. The number of vertical segments within the path is $i \geqslant 0$, registering the path as a member in a group of paths of order i. Consider first the collection of all paths of the group $i = 0$. This collection comprises diagonal segments only, yielding the highest power of $-\gamma^2$. For observation point B, one such path traces half the perimeter of the rhombus at either side, contributing the γ^8 factor as the highest power for the case of Fig. 3. The collection of paths of the opposite extreme case, yielding γ^0, contains only one path, i.e., the vertical straight line connecting the initial and observation points A and B, respectively. Intermediate powers of $-\gamma^2$ are produced by paths with a varying number of vertical (and hence diagonal) segments. The problem of finding the field at observation point B as an outcome of initial point A thus translates into finding the number of different paths within a collection of the same power of $-\gamma^2$. The result will take the form a finite power series in $-\gamma^2$.

As an example, consider the evaluation of the field at observation point C in Fig. 4 as a function of the field at the initial point A. Three collections of paths between the points A and C can be identified with $i = 0$ (diagonal segments only), $i = 1$ (one vertical segment), and $i = 2$ (two vertical segments) as shown in Fig. 5. The total path counts are 15, 20 and 6, for the three collections. There are no paths with vertical segments only in this case. The resultant formula for the Green's function is then

$$E_x|_{k=1}^{n=3} = E_x|_{k=0}^{n=0} \cdot (15\gamma^6 - 20\gamma^4 + 6\gamma^2). \tag{4}$$

In order to formulate a general procedure for counting the number of paths within each group, we define the path count vector (PCV) comprising components of different orders at any observation point. At the observation point B, the PCV is $\mathbf{b} = (b_0, b_1, b_2, \ldots, b_i)$. Each one of the PCV components b_i is a combination of similar components of $\mathbf{x} = (x_0, x_1, x_2, \ldots, x_i)$, $\mathbf{y} = (y_0, y_1, y_2, \ldots, y_i)$ and $\mathbf{z} = (z_0, z_1, z_2, \ldots, z_i)$, where $\mathbf{y}$ is the PCV at Y on the vertical straight path, and $\mathbf{x}$ and $\mathbf{z}$ are at X and Z on the left and right diagonals leading to B, respectively, as seen in Figs. 3 and 6. These combinations are

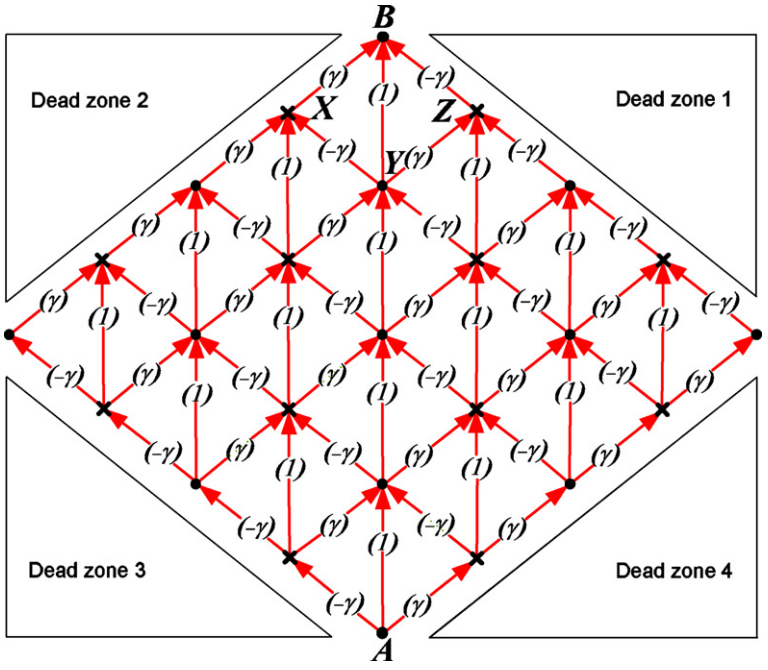

Fig. 3. Spatial–temporal grid with structure of paths leading to point B.

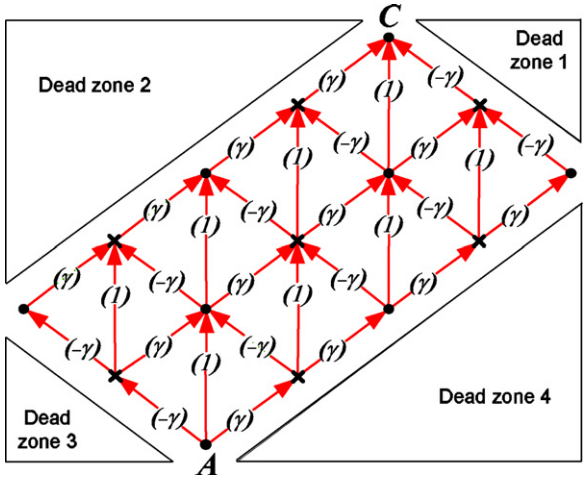

Fig. 4. Spatial–temporal grid with structure of paths leading from point A to point C.

$$
\begin{aligned}
b_0 &= x_0 + z_0 \\
b_1 &= x_1 + z_1 + y_0 \\
&\vdots \\
b_{i-1} &= x_{i-1} + z_{i-1} + y_{i-2} \\
b_i &= y_{i-1}
\end{aligned}
\tag{5}
$$

This procedure can be applied to all points in the spatial–temporal grid of Fig. 3. The PCVs for all points for a signal originating at the initial point A are marked in Fig. 7. The PCV components, as seen in the figure, have

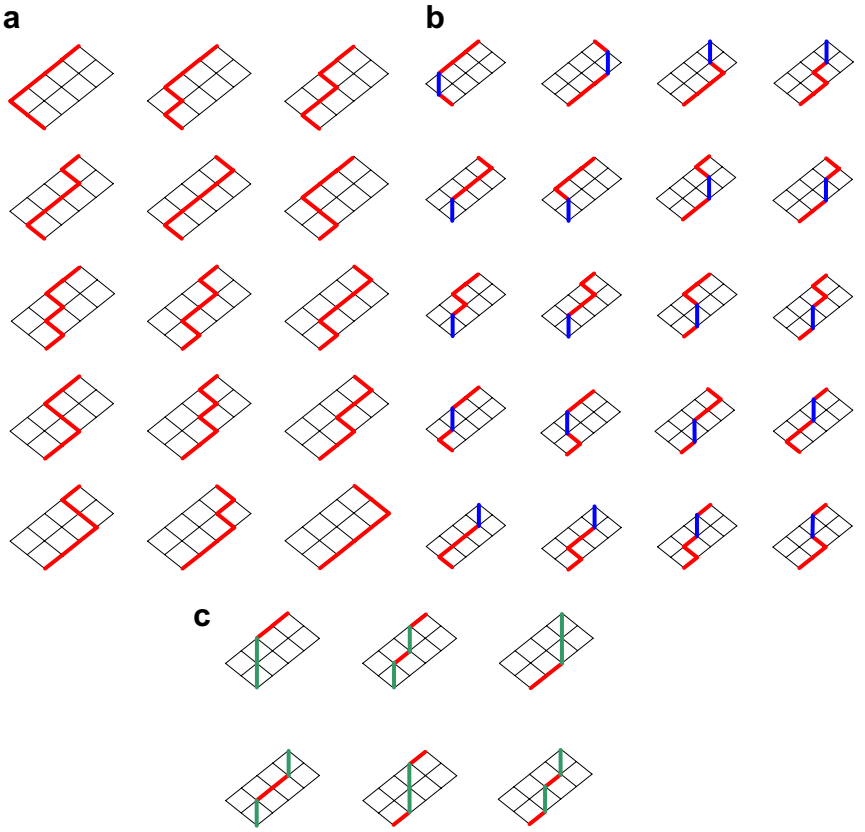

Fig. 5. Collection of between initial point A and observation point C in Fig. 4: (a) 15 paths with diagonal segments only, (b) 20 paths with one vertical segment and (c) 6 paths with two vertical segments.

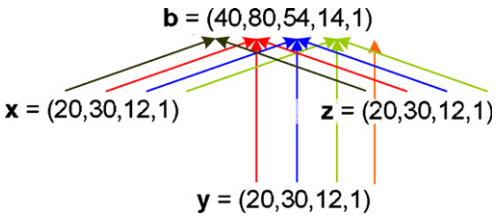

Fig. 6. Path count vectors (PCVs) leading to point B whose combination is given by **b** (see also Eq. (5)). The PCV components are associated with different powers of $-\gamma^2$.

been found by straightforward counting at this stage. However, the main goal of this work is a general formulations as given below.

3. Combinatorial development

3.1. Aperture excited by magnetic current: the Catalan triangle and its modification

We first address the aperture problem defined in Eq. (2a). Considering Fig. 8, we define Γ as the half space $z > 0$, with the aperture $\partial\Gamma_\alpha$ being the straight line $k = \frac{1}{2}$ and supporting a magnetic impulsive current source J_m backed by a perfect electric conductor (PEC), i.e., the problem is wholly formulated by the following reduction of Eq. (2a):

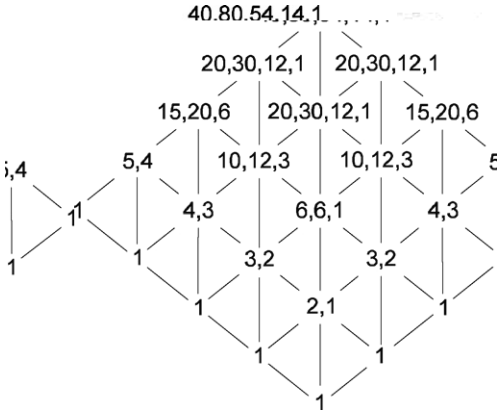

Fig. 7. Path count vectors (PCVs) for all points in the space–time grid for a signal originating at the initial point A.

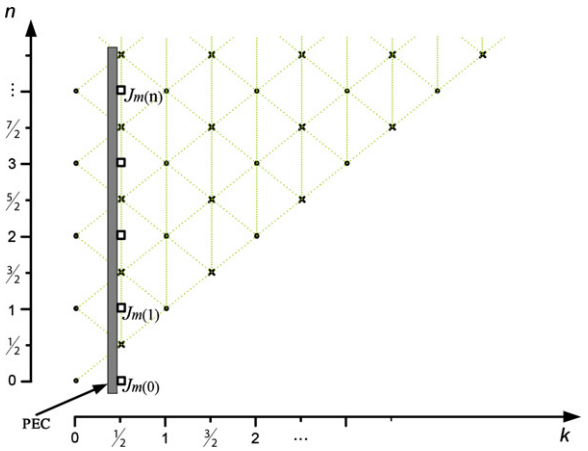

Fig. 8. Aperture excited by magnetic current.

$$E_x(z,t) = \int_{t'} J^{\mathrm{eq}}_{msy}(z_\alpha, t') \frac{\partial G_e(z - z_\alpha; t - t')}{\partial z'} \mathrm{d}t'. \tag{6}$$

One can regard this current as an equivalent source, representing an electric aperture field E_a sampled at $k = 0$, as shown in Fig. 9. Solving for the PCVs in this case results in modified Catalan numbers (MCNs), where the unmodified Catlan numbers form the Catalan triangle [15], as shown below.

As a first step, consider the $i = 0$ component of the PCV. The solution for this problem is embodied in the Catalan numbers

$$C_{l,m} = \frac{(l+m)!(l-m+1)}{m!(l+1)!} \tag{7}$$

that form triangle in its conventional form (see Fig. 10). The numbers are interrelated by the recursive relationship

$$C_{l,m} = C_{l-1,m} + C_{l,m-1}; \quad 0 \leqslant m \leqslant l. \tag{8}$$

Using a simple transformation, the indices (l,m) are traded for (n,k), the latter pair coinciding with the conventional spatial–temporal pair:

$$\mathcal{C}_{n,k} = \frac{(2n)!(2k+1)}{(n-k)!(n+k+1)!}, \quad \begin{array}{l} k \leqslant n \\ (n,k) \in \{0,1,2,\ldots\} \quad \text{or} \\ (n,k) \in \left\{\frac{1}{2}, \frac{3}{2}, \ldots\right\} \end{array} \tag{9}$$

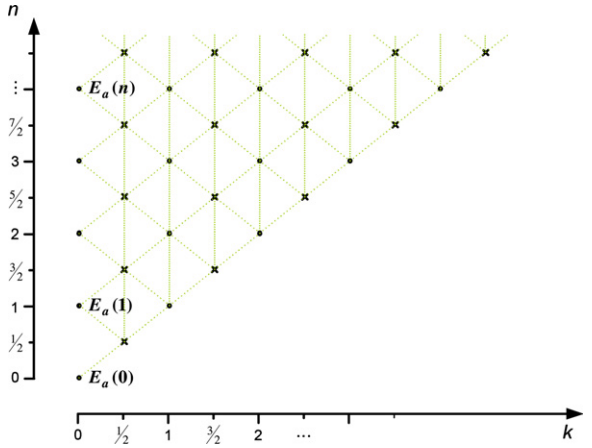

Fig. 9. Equivalent aperture with electric field.

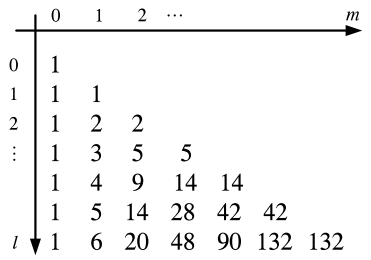

Fig. 10. The Catalan triangle.

The $\mathcal{C}_{n,k}$ numbers form a tilted and flipped modification of the Catalan triangle shown in Fig. 11. The PCV component for $0 < i \leqslant n$ are the MCNs denoted $\mathcal{R}^i_{n,k}$, that have the added dimension provided by the index i. In view of Fig. 6, the MCNs are equal to the summation of the PCVs of the left diagonal, right diagonal and vertical adjacent initial points of orders i, i and $i-1$, respectively. Added together, they comprise Eq. (10) as follows:

$$\mathcal{R}^i_{n,k} = \mathcal{R}^i_{n-\frac{1}{2},k-\frac{1}{2}} + \mathcal{R}^i_{n-\frac{1}{2},k+\frac{1}{2}} + \mathcal{R}^{i-1}_{n-1,k}, \tag{10a}$$

$$n \geqslant 0, \quad k \geqslant 0, \quad i \geqslant 0 \tag{10b}$$

$$k \leqslant n \tag{10c}$$

$$\leqslant n - k + 1 \tag{10d}$$

with $(n,k) \in \{0,1,2,\ldots\}$ or $(n,k) \in \{\frac{1}{2},\frac{3}{2},\ldots\}$. The boundary and initial conditions are

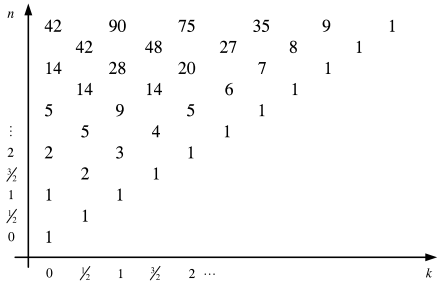

Fig. 11. Flipped and tilted Catalan triangle.

$$\mathcal{R}^0_{n,n+1} = \mathcal{R}^0_{n,-\frac{1}{2}} = \mathcal{R}^{-1}_{n,k} = 0 \quad \text{and} \quad \mathcal{R}^0_{0,0} = 1, \tag{11}$$

respectively.

Eqs. (10)–(11) can be used to compute the path count numerically. While the computations complexity of implementing (10) is of the same order of the conventional FDTD, note that this computation is independent of both the source and γ, therefore it can be performed beforehand for many problems related to a given geometry. In the one-dimensional aperture and free space models, treated in this Section and in Section 3.2, respectively, a closed form evaluation using combinatorial considerations is developed below.

For an arbitrary i, the MCNs are given by

$$\mathcal{R}^i_{n,k} = \frac{(2n-i)!(2k+1)}{i!(n-k-i)!(n+k-i+1)!} \tag{12}$$

as can be proven by mathematical induction. Note that the special case $i = 0$ coincides with Eq. (10). As mentioned above, the MCNs provided by Eq. (12) are used as the coefficient in the weighted summation of powers of $-\gamma^2$ to construct the DGF, as detailed in Section 2. The lowest order MCNs appear in Fig. 12.

3.2. Source problem in free space: application of the Pascal triangle and its modification

The free space model of Eq. (2b) is treated next. Consider the case of an electric current source only, for which (2b) reduces to

$$E_x(z,t) = \mu \frac{\partial}{\partial t} \int \int_{z'=z_\alpha,t'}^{z'=z_\beta} J(z',t') G_e(z-z';t-t') \mathrm{d}z' \, \mathrm{d}t'. \tag{13}$$

For a planar source at $z = 0$ exciting the entire free space $k \lessgtr 0$, one notes that all the PCVs with $i > 0$ are modified Pascal numbers (MPNs) obeying the following recursive rule, (see Figs. 2 and 6 and Eq. (5)):

$$\mathcal{P}^i_{n,k} = \mathcal{P}^i_{n-\frac{1}{2},k-\frac{1}{2}} + \mathcal{P}^i_{n-\frac{1}{2},k+\frac{1}{2}} + \mathcal{P}^{i-1}_{n-1,k} \tag{14a}$$

$$n \geqslant 0, \quad i \geqslant 0 \tag{14b}$$

$$|k| \leqslant n \tag{14c}$$

$$i \leqslant n + 1 - |k|, \tag{14d}$$

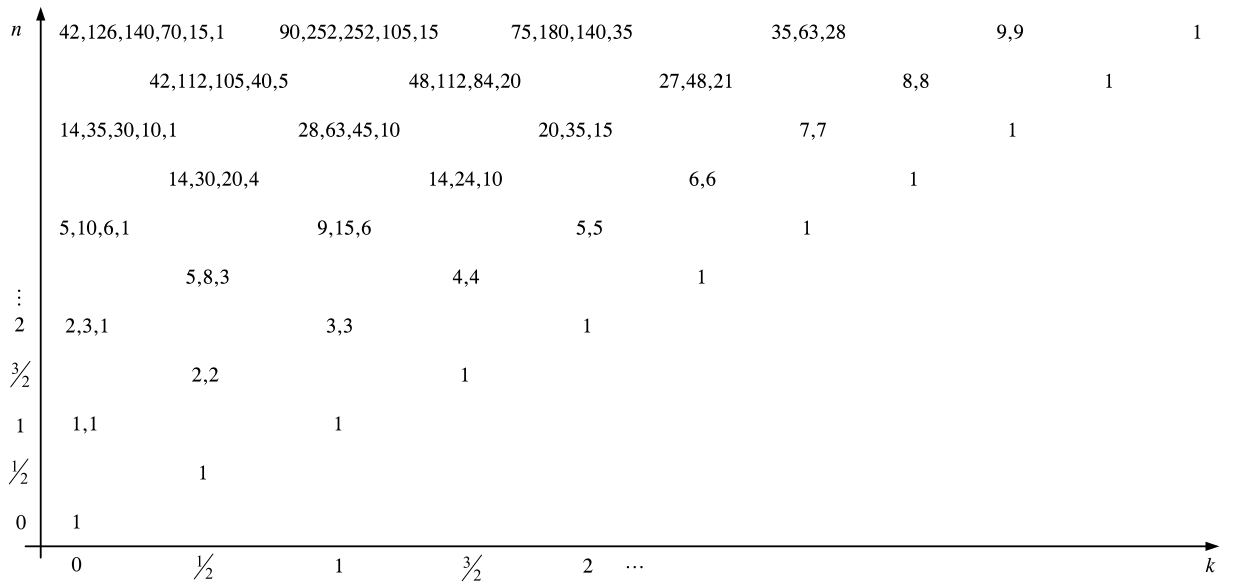

Fig. 12. Lowest order PCVs in the time-space region as modified Catalan numbers.

with $\{n \in \{0,+1,\ldots\}$ and $k \in \{0,\pm 1,\ldots\}\}$ or $\{n \in \{+\frac{1}{2},+\frac{3}{2},\ldots\}$ and $k \in \{\pm\frac{1}{2},\pm\frac{3}{2},\ldots\}\}$. The boundary and the initial conditions are

$$\mathcal{P}^0_{n,n+1} = \mathcal{P}^0_{n,-n-1} = \mathcal{P}^{-1}_{n,k} = 0, \quad \text{and} \quad \mathcal{P}^0_{0,0} = 1, \tag{15}$$

respectively. The recursive Eq. (14) is solved to yield the following MPNs:

$$\mathcal{P}^i_{n,k} = \frac{(2n-i)!}{i!(n-k-i)!(n+k-i)!}. \tag{16}$$

For $\gamma = 1$, we have $\sum_{i=0}^{n-k}(-1)^i R^i_{n,k} = 1, k \leqslant n$, as can also be seen by inspection of Fig. 7. This formulation is still to be adapted to physical scenarios.

Two-dimensional formulation. An initial generalization to two dimensions is as follows. A four sided pyramid is built from two Pascal triangles, with its apex at the origin of the spatial–temporal coordinates. The pyramid comprises 2D modified Pascal numbers $\mathcal{H}^i_{n,k,p}$, adhering to the following generalization of (14):

$$\mathcal{H}^i_{n,k,p} = \mathcal{H}^i_{n-\frac{1}{2},k-\frac{1}{2},p} + \mathcal{H}^i_{n-\frac{1}{2},k+\frac{1}{2},p} + \mathcal{H}^i_{n-\frac{1}{2},k,p-\frac{1}{2}} + \mathcal{H}^i_{n-\frac{1}{2},k,p+\frac{1}{2}} + \mathcal{H}^{i-1}_{n-1,k,p} \tag{17}$$

with $x = k\Delta x$, $y = p\Delta y$. Its solution is the generalization of (16) into two dimensions:

$$\mathcal{H}^i_{n,k,p} = \frac{(2n-2i)!(2n-i)!}{i!(n+k+p-i)!(n-k+p-i)!(n+k-p-i)!(n-k-p-i)!}, \quad 0 \leqslant p,k \leqslant n. \tag{18}$$

At this point, this solution requires adaptation to either the TE or TM case.

3.3. Evaluation of the Green's function for the aperture case using modified Catalan numbers

Consider the aperture problem of Section 3.1 with an electric field at $k = 0$ and its equivalent magnetic current at $k = \frac{1}{2}$, (see Fig. 9 and a representative waveform at the left of Fig. 13). A bounded trapezoidal region that contains all paths of the propagating field is identified, as shown in the figure. This trapezoid is depicted for the temporal duration $n = (0\text{–}8)$. Note that for general location (n,k) within the trapezoid, E^n_k involves convolutions of the spatial–temporal source vector with the DGF[1]; e.g., $E^{n=8}_{k=5}$ contains the contribution from the source vector containing the components $E_a(n)$,$n = 0$, 1, 2, 3. For example, Fig. 14 shows the contributions from $E_a(0)$ to the observation point (8, 5), expressed as the following weighted summation over powers of $-\gamma^2$ with the PCVs as the coefficients:

$$E^{n=8}_{k=5}\{\text{from } E_a(0)\} = \underbrace{E_a(0)(-\gamma)}_{\text{from } k=0 \text{ to } k=\frac{1}{2}} \Bigg(\overbrace{\underbrace{\mathscr{R}^{i=0}_{8-\frac{1}{2},5-\frac{1}{2}}}_{\text{Number of paths}} \cdot \underbrace{(-\gamma)^{2\left(5-\frac{1}{2}\right)}}_{\text{from } \left(\frac{1}{2},\frac{1}{2}\right) \text{ to } (5,5)} \cdot \underbrace{(-\gamma^2)^{(8-5-0)}}_{\text{from } (5,5) \text{ to } (5,8)}}^{\text{Paths With Diagonals Only}} +$$

$$\overbrace{\underbrace{\mathscr{R}^{i=1}_{8-\frac{1}{2},5-\frac{1}{2}}}_{} \cdot \underbrace{(-\gamma)^{2\left(5-\frac{1}{2}\right)}}_{} \cdot \underbrace{(-\gamma^2)^{(8-5-1)}}_{}}^{\text{Paths With Diagonals And One Vertical}} + \tag{19}$$

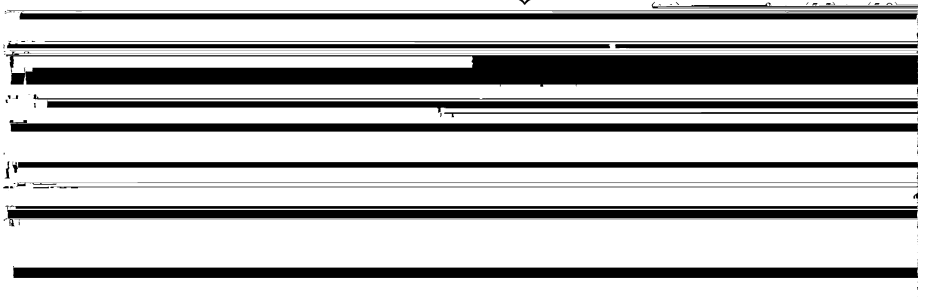

[1] E^n_k is now used as a shorthand for $E_x|^n_k$.

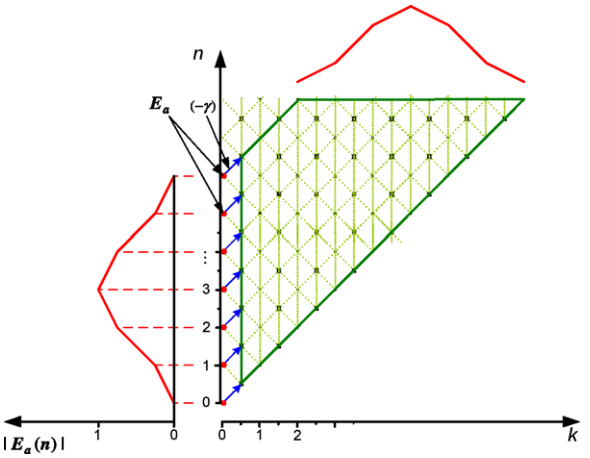

Fig. 13. Region of propagation characteristics for the aperture problem.

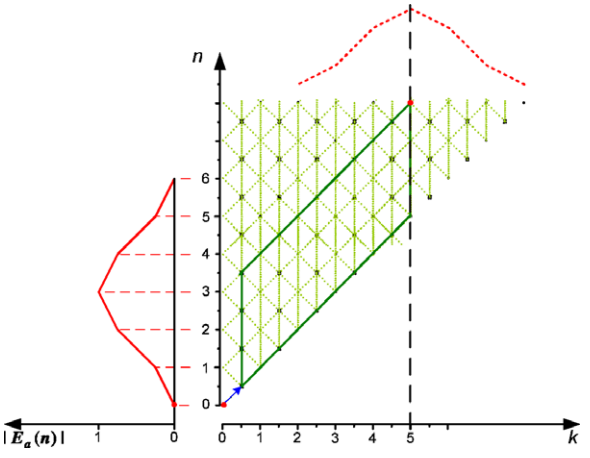

Fig. 14. Finding the field at $n = 8$, $k = 5$ as a function of the excitation at the zero position at $n = 0$.

A similar weighted summation for the case $E_a(1)$ takes the form

$$E_{k=5}^{n=8}\ \{\text{from } E_a(1)\} = \underbrace{E_a(1)(-\gamma)}_{\text{from } k=0 \text{ to } k=\frac{1}{2}} \left(\overbrace{\underbrace{\mathcal{R}_{8-1-\frac{1}{2},5-\frac{1}{2}}^{i=0}}_{\text{Number of paths}} \cdot \underbrace{(-\gamma)^{2\left(5-\frac{1}{2}\right)}}_{\text{from } \left(\frac{1}{2},\frac{1}{2}\right) \text{ to } (5,5)} \cdot \underbrace{(-\gamma^2)^{(8-5-1-0)}}_{\text{from } (5,5) \text{ to } (8,8)}}^{\text{Paths With Diagonals Only}} + \right.$$

$$\overbrace{\underbrace{\mathcal{R}_{8-1-\frac{1}{2},5-\frac{1}{2}}^{i=1}}_{\text{Number of paths}} \cdot \underbrace{(-\gamma)^{2\left(5-\frac{1}{2}\right)}}_{\text{from } \left(\frac{1}{2},\frac{1}{2}\right) \text{ to } (5,5)} \cdot \underbrace{(-\gamma^2)^{(8-5-1-1)}}_{\text{from } (5,5) \text{ to } (8,8)}}^{\text{Paths With Diagonals And One Vertical}} +$$

$$\left. \overbrace{\underbrace{\mathcal{R}_{8-1-\frac{1}{2},5-\frac{1}{2}}^{i=2}}_{\text{Number of paths}} \cdot \underbrace{(-\gamma)^{2\left(5-\frac{1}{2}\right)}}_{\text{from } \left(\frac{1}{2},\frac{1}{2}\right) \text{ to } (5,5)} \cdot \underbrace{(-\gamma^2)^{(8-5-1-2)}}_{\text{from } (5,5) \text{ to } (8,8)}}^{\text{Paths With Diagonals And Two Verticals}} \right) \tag{20}$$

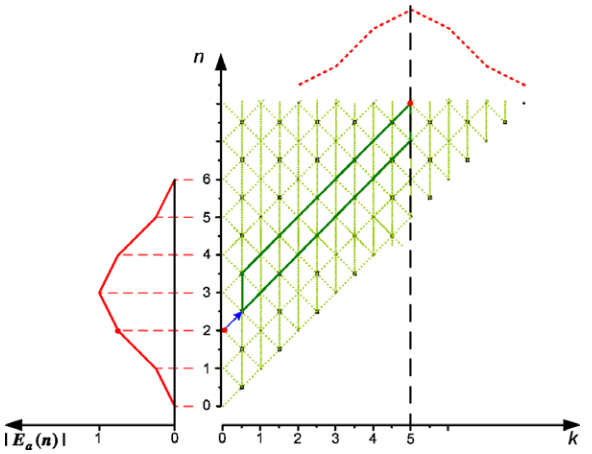

Fig. 15. Finding the field at $n = 8$, $k = 5$ as a function of the excitation at the zero position at $n = 2$.

The case $n = 2$ is shown in Fig. 15. Finally, the trapezoid representing the contribution by $E_a(3)$ to point $(n = 8, k = 5)$ degenerates to a straight line, with the pertinent equation being

$$E_{k=5}^{n=8}\{\text{from } E_a(3)\} = \underbrace{E_a(3)(-\gamma)}_{\text{from } k=0 \text{ to } k=\frac{1}{2}} \cdot \overbrace{\Big[\underbrace{\mathcal{R}^{i=0}_{8-3-\frac{1}{2},5-\frac{1}{2}}}_{\text{Number of paths}} \cdot \underbrace{(-\gamma)^{2\left(5-\frac{1}{2}\right)}}_{\text{from } \left(\frac{1}{2},\frac{1}{2}\right) \text{ to } (5,5)} \cdot \underbrace{(-\gamma^2)^{(8-5-3-0)}}_{\text{from } (5,5) \text{ to } (5,8)}\Big]}^{\text{Paths With Diagonals Only}}. \tag{21}$$

One can now assemble all the above contributions, arriving at

$$E_k^n = \sum_{m=0}^{n-k} E_0^m(-\gamma) \cdot \left[\sum_{i=0}^{n-m-k} \mathcal{R}^i_{n-m-\frac{1}{2},k-\frac{1}{2}} \cdot (-\gamma)^{2\left(k-\frac{1}{2}\right)} \cdot (-\gamma^2)^{n-m-k-i}\right], \quad k \geqslant \frac{1}{2} \tag{22}$$

(the case $k = 0$ indicates the given aperture field). This equation can be cast in the form of a convolution of the spatial–temporal source vector with the DGF as follows:

$$E_k^n = \sum_{m=0}^{n-k} E_0^m G_k^{n,m} = \begin{pmatrix} E_0^0 & E_0^1 & \cdots & E_0^{n-k} \end{pmatrix} \begin{pmatrix} G_k^{n,0} \\ G_k^{n,1} \\ \vdots \\ G_k^{n,n-k} \end{pmatrix}; \quad k \geqslant \frac{1}{2}, \tag{23}$$

where a typical Green's function component is defined as the following convolution expression:

$$G_k^{n,m} = (-1)^k \sum_{i=0}^{n-m-k} \mathcal{R}^i_{n-m-\frac{1}{2},k-\frac{1}{2}} (-\gamma^2)^{n-m-i}. \tag{24}$$

Transferring Eq. (23) into matrix form, define now the DGF vector comprising the components defined in (24):

$$(\mathbf{G}_k^n)^t \triangleq \begin{pmatrix} G_k^{n,0} \\ G_k^{n,1} \\ \vdots \\ G_k^{n,n-k} \end{pmatrix} = \begin{pmatrix} \sum_{i=0}^{n-k} \mathcal{R}^i_{n-\frac{1}{2},k-\frac{1}{2}}(-1)^{-k}(-\gamma^2)^{n-i} \\ \sum_{i=0}^{n-k-1} \mathcal{R}^i_{n-\frac{3}{2},k-\frac{1}{2}}(-1)^{-k}(-\gamma^2)^{n-i-1} \\ \sum_{i=0}^{n-k-2} \mathcal{R}^i_{n-\frac{5}{2},k-\frac{1}{2}}(-1)^{-k}(-\gamma^2)^{n-i-2} \\ \vdots \\ \sum_{i=0}^{0} \mathcal{R}^i_{k-\frac{1}{2},k-\frac{1}{2}}(-1)^{-k}(-\gamma^2)^{k-i} \end{pmatrix} \tag{25}$$

where $(\mathbf{G}_k^n)^t$ denotes the transpose of the row vector $\mathbf{G}_k^n$, such that

$$E_k^n = \mathbf{G}_k^n \cdot \begin{pmatrix} E_0^0 \\ E_0^1 \\ \vdots \\ E_0^{n-k} \end{pmatrix}. \tag{26}$$

The detailed Eq. (25) shows the form of another level of convolution

$$\mathbf{G}_k^n = \begin{pmatrix} [(-1)^{n-k}]\gamma^{2(n)} \\ [(-1)^{n-k-1}]\gamma^{2(n-1)} \\ [(-1)^{n-k-2}]\gamma^{2(n-2)} \\ \vdots \\ [(-1)^{0}]\gamma^{2(k)} \end{pmatrix}^t \cdot \begin{pmatrix} \mathcal{R}^0_{n-\frac{1}{2},k-\frac{1}{2}} & 0 & 0 & \dots & 0 \\ \mathcal{R}^1_{n-\frac{1}{2},k-\frac{1}{2}} & \mathcal{R}^0_{n-\frac{3}{2},k-\frac{1}{2}} & 0 & \dots & 0 \\ \mathcal{R}^2_{n-\frac{1}{2},k-\frac{1}{2}} & \mathcal{R}^1_{n-\frac{3}{2},k-\frac{1}{2}} & \mathcal{R}^0_{n-\frac{5}{2},k-\frac{1}{2}} & \dots & 0 \\ \vdots & \vdots & \vdots & \ddots & \vdots \\ \mathcal{R}^{n-k}_{n-\frac{1}{2},k-\frac{1}{2}} & \mathcal{R}^{n-k-1}_{n-\frac{3}{2},k-\frac{1}{2}} & \mathcal{R}^{n-k-2}_{n-\frac{5}{2},k-\frac{1}{2}} & \dots & \mathcal{R}^0_{k-\frac{1}{2},k-\frac{1}{2}} \end{pmatrix}. \tag{27}$$

The field over the entire region after n time steps, resulting from a temporal pulse at $k = 0$, is

$$\begin{matrix} E_1^n \\ E_2^n \\ \vdots \\ E_k^n \end{matrix} = \begin{pmatrix} \overbrace{\begin{matrix} (\mathbf{G}_1^n & \dots & \dots & \dots &) \\ (\mathbf{G}_2^n & \dots & \dots &) & 0 \\ (\mathbf{G}_3^n & \dots &) & 0 & 0 \\ \vdots & & & \vdots & \vdots \\ (\mathbf{G}_{k-1}^n &) & 0 & \dots & 0 \end{matrix}}^{\text{length } n} \\ \underbrace{\begin{matrix} (\mathbf{G}_k^n) & 0 & 0 & \dots & 0 \end{matrix}}_{\text{length } k} \end{pmatrix} \cdot \begin{pmatrix} E_0^0 \\ E_0^1 \\ \vdots \\ E_0^{n-k} \\ \vdots \\ E_0^{n-1} \end{pmatrix} \tag{28}$$

where the vectors $\mathbf{G}_k^n$ were indicated in Eq. (27). Their sizes depend upon the spatial–temporal separation between initial and observation points, ranging from a maximum of n for E_1^n to a minimum of $n - k$ for E_k^n. The temporal field at the spatial point k as a function of a temporal pulse at $k = 0$ is

$$\begin{pmatrix} E_k^0 \\ E_k^1 \\ \vdots \\ E_k^n \end{pmatrix} = \begin{pmatrix} & & & & & \\ 0 & 0 & 0 & \cdots & 0 & 0 \\ \vdots & \ddots & \ddots & \ddots & 0 & 0 \\ 0 & 0 & \dots & 0 & 0 & 0 \\ (\mathbf{G}_k^k) & 0 & 0 & \dots & 0 & 0 \\ (\mathbf{G}_k^{k+1} &) & 0 & \dots & 0 & 0 \\ \vdots & \ddots & \ddots & \ddots & \ddots & 0 \\ (\mathbf{G}_k^{n-2} & \dots & \dots &) & 0 & 0 \\ (\mathbf{G}_k^{n-1} & \dots & \dots & \dots &) & 0 \\ \underbrace{(\mathbf{G}_k^n}_{\text{length } n-k} & \dots & \dots & \dots & \dots &) \end{pmatrix} \cdot \begin{pmatrix} E_0^0 \\ E_0^1 \\ \vdots \\ E_0^{n-k} \end{pmatrix} \tag{29}$$

A companion formulation for the magnetic field can be obtained along similar lines.

3.4. Recursive method for calculating field points using MCNs

In this section, an efficient evaluation of the electric field via the convolution of the source with $G_k^{n,m}$ (Section 3.3) is described. To this end, we start with the explicit expression for Eq. (24) for, say, $m = 0$ (see the first column of $\mathbf{G}_k^n$ in Eq. (27)):

$$\begin{aligned} G_k^{n,0} &= \begin{pmatrix} [(-1)^{n-k}]\gamma^{2(n)} \\ [(-1)^{n-k-1}]\gamma^{2(n-1)} \\ [(-1)^{n-k-2}]\gamma^{2(n-2)} \\ \cdots \\ [(-1)^0]\gamma^{2(k)} \end{pmatrix}^t \cdot \begin{pmatrix} \mathcal{R}^0_{n-\frac{1}{2},k-\frac{1}{2}} \\ \mathcal{R}^1_{n-\frac{1}{2},k-\frac{1}{2}} \\ \mathcal{R}^2_{n-\frac{1}{2},k-\frac{1}{2}} \\ \vdots \\ \mathcal{R}^{n-k}_{n-\frac{1}{2},k-\frac{1}{2}} \end{pmatrix} = \begin{pmatrix} [(-1)^0]\gamma^{2(k)} \\ \cdots \\ [(-1)^{n-k-2}]\gamma^{2(n-2)} \\ [(-1)^{n-k-1}]\gamma^{2(n-1)} \\ [(-1)^{n-k}]\gamma^{2(n)} \end{pmatrix}^t \cdot \begin{pmatrix} \mathcal{R}^{n-k}_{n-\frac{1}{2},k-\frac{1}{2}} \\ \vdots \\ \mathcal{R}^2_{n-\frac{1}{2},k-\frac{1}{2}} \\ \mathcal{R}^1_{n-\frac{1}{2},k-\frac{1}{2}} \\ \mathcal{R}^0_{n-\frac{1}{2},k-\frac{1}{2}} \end{pmatrix} \\ &= \gamma^{2k}\mathcal{R}^{n-k}_{a,b} - \gamma^{2(k+1)}\mathcal{R}^{n-k-1}_{a,b} + \gamma^{2(k+2)}\mathcal{R}^{n-k-2}_{a,b} \cdots \mp \gamma^{2(n-1)}R^1_{a,b} \pm \gamma^{2(n)}\mathcal{R}^0_{a,b}. \end{aligned} \tag{30}$$

with $(a,b) = \left(n-\frac{1}{2}, k-\frac{1}{2}\right)$. Computation of the MCNs in (30) poses the challenge of high computational complexity due to rapid growth of the MCNs with k and n (see Eq. (12) and Fig. 12). In order to overcome this obstacle, one can reorder the algebraic operations in the last line of Eq. (30) as follows:

$$\begin{aligned} G_k^{n,0} &= \mathcal{R}^{n-k}_{a,b} \cdot \gamma^{2k}\left(1 - \frac{\mathcal{R}^{n-k-1}_{a,b}}{\mathcal{R}^{n-k}_{a,b}} \cdot \gamma^2 + \frac{\mathcal{R}^{n-k-2}_{a,b}}{\mathcal{R}^{n-k}_{a,b}} \cdot \gamma^4 - \cdots \pm \frac{\mathcal{R}^0_{a,b}}{\mathcal{R}^{n-k}_{a,b}} \cdot \gamma^{2(n-k)}\right) \\ &= \mathcal{R}^{n-k}_{a,b} \cdot \gamma^{2k}\left(1 - \frac{\mathcal{R}^{n-k-1}_{a,b}}{\mathcal{R}^{n-k}_{a,b}} \cdot \gamma^2\left(1 - \frac{\mathcal{R}^{n-k-2}_{a,b}}{\mathcal{R}^{n-k-1}_{a,b}} \cdot \gamma^2\left(1 - \cdots \gamma^2\left(1 - \frac{\mathcal{R}^0_{a,b}}{\mathcal{R}^1_{a,b}} \cdot \gamma^2\right)\cdots\right)\right)\right). \end{aligned} \tag{31}$$

Define

$$\mathcal{N}^i_{a,b} \triangleq \frac{\mathcal{R}^i_{a,b}}{\mathcal{R}^{i+1}_{a,b}} = \frac{\dfrac{(2a-i)!(2b+1)}{i!(a-b-i)!(a+b-i+1)!}}{\dfrac{(2a-i-1)!(2b+1)}{(i+1)!(a-b-i-1)!(a+b-i)!}} = \frac{(i+1)(2a-i)}{(a-b-i)(a+b-i+1)} \tag{32}$$

and augment (31) to obtain the entire the Green vector (Eq. (25)) as follows:

$$(\mathbf{G}_k^n)^t = \gamma^{2k}\begin{pmatrix} \mathcal{R}^{n-k}_{n-\frac{1}{2},k-\frac{1}{2}}\mathcal{T}^{n-k}_{n-\frac{1}{2},k-\frac{1}{2}} \\ \mathcal{R}^{n-k-1}_{n-\frac{3}{2},k-\frac{1}{2}}\mathcal{T}^{n-k-1}_{n-\frac{3}{2},k-\frac{1}{2}} \\ \vdots \\ \mathcal{R}^{1}_{k+\frac{1}{2},k-\frac{1}{2}}\mathcal{T}^{1}_{k+\frac{1}{2},k-\frac{1}{2}} \\ \mathcal{R}^{0}_{k-\frac{1}{2},k-\frac{1}{2}}\mathcal{T}^{0}_{k-\frac{1}{2},k-\frac{1}{2}} \end{pmatrix} \tag{33}$$

where

$$\mathcal{T}^{n-k}_{(a,b)} = 1 - \mathcal{N}^{n-k-1}_{a,b}\gamma^2(1 - \mathcal{N}^{n-k-2}_{a,b}\gamma^2(1 - \cdots\gamma^2(1 - \mathcal{N}^{0}_{a,b}\gamma^2)\cdots)) \tag{34}$$

with $\mathcal{T}^0_{k-\frac{1}{2},k-\frac{1}{2}} = 1$ and $\mathcal{R}^0_{k-\frac{1}{2},k-\frac{1}{2}} = 1$. Using (33) with (26), one has

$$E_k^n = \gamma^{2k}\left[\mathcal{R}^0_{k-\frac{1}{2},k-\frac{1}{2}}\mathcal{T}^0_{k-\frac{1}{2},k-\frac{1}{2}}E_0^{n-k} + \mathcal{R}^1_{k+\frac{1}{2},k-\frac{1}{2}}\mathcal{T}^1_{k+\frac{1}{2},k-\frac{1}{2}}E_0^{n-k-1} + \cdots + \mathcal{R}^{n-k-1}_{n-\frac{3}{2},k-\frac{1}{2}}\mathcal{T}^{n-k-1}_{n-\frac{3}{2},k-\frac{1}{2}}E_0^1 + \mathcal{R}^{n-k}_{n-\frac{1}{2},k-\frac{1}{2}}\mathcal{T}^{n-k}_{n-\frac{1}{2},k-\frac{1}{2}}E_0^0\right] \tag{35}$$

Again, reordering the algebraic operation in Eq. (35) in the same manner as Eq. (32), we have

$$E_k^n = \mathcal{R}^0_{k-\frac{1}{2},k-\frac{1}{2}}\cdot\gamma^{2k} \cdot\left(E_0^{n-k} + \frac{\mathcal{R}^1_{k+\frac{1}{2},k-\frac{1}{2}}}{\mathcal{R}^0_{k-\frac{1}{2},k-\frac{1}{2}}}\cdot\ldots\cdot\left(\mathcal{T}^{n-k-2}_{k+\frac{1}{2},k-\frac{1}{2}}\cdot E_0^2 + \frac{\mathcal{R}^{n-k-1}_{n-\frac{3}{2},k-\frac{1}{2}}}{\mathcal{R}^{n-k-2}_{n-\frac{5}{2},k-\frac{1}{2}}}\cdot\left(\mathcal{T}^{n-k-1}_{n-\frac{3}{2},k-\frac{1}{2}}\cdot E_0^1 + \frac{\mathcal{R}^{n-k}_{n-\frac{1}{2},k-\frac{1}{2}}}{\mathcal{R}^{n-k-1}_{n-\frac{3}{2},k-\frac{1}{2}}}\cdot\mathcal{T}^{n-k}_{n-\frac{1}{2},k-\frac{1}{2}}\cdot E_0^0\right)\right)\ldots\right) \tag{36}$$

Defining $\mathcal{M}^i_{a,b} \triangleq \frac{\mathcal{R}^i_{a,b}}{\mathcal{R}^{i-1}_{a-1,b}} = \frac{(2a-i)}{i}$ and using $\mathcal{R}^0_{k-\frac{1}{2},k-\frac{1}{2}} = 1$, we finally arrive at Eq. (37) that contains no factorials, thus affording a very efficient two-dimensional recursive computation of the Green's function - source convolution (12):

$$E_k^n = \gamma^{2k}\left(E_0^{n-k} + \mathcal{M}^1_{k+\frac{1}{2},k-\frac{1}{2}}\ldots\left(\mathcal{T}^{n-k-2}_{k+\frac{1}{2},k-\frac{1}{2}}E_0^2 + \mathcal{M}^{n-k-1}_{n-\frac{3}{2},k-\frac{1}{2}}\left(\mathcal{T}^{n-k-1}_{n-\frac{3}{2},k-\frac{1}{2}}E_0^1 + \mathcal{M}^{n-k}_{n-\frac{1}{2},k-\frac{1}{2}}\mathcal{T}^{n-k}_{n-\frac{1}{2},k-\frac{1}{2}}E_0^0\right)\right)\ldots\right) \tag{37}$$

Note that for the case $\gamma = 1$ in Eq. (27), one can show that

$$R^0_{n,k} = 1, \quad k = n \tag{38a}$$

$$\sum_{i=0}^{n-k}(-1)^i R^i_{n,k} = 0, \quad k < n \tag{38b}$$

that can also be verified by inspection of Fig. 12. Therefore, in this case $E_k^n = \sum_{l=0}^{n-k}E_0^l\cdot\delta_{i,n-k} = E_0^{n-k}$ as expected for the dispersion-free case.

3.5. Assessment of computational complexity as compared with the FDTD

Since the DGF can also be computed by the straightforward FDTD method, the question of possible computational advantages of either method arises. The first factor in favor of the this analytical approach is the fact that the once the coefficients have been found, the DGF is available for all values of γ and all sources, while the FDTD computation needs to be repeated for each of these values. The analytical method then has an edge that depends on the required flexibility in the use of γ and thus cannot be quantified. Another factor is related to pulse width relative to the distance traversed by the pulse. Consider a pulse that is quite narrow such that most of the information is contained in the area around the characteristic $k = n$. For $k = n$, we have only one diagonal path, representing a single γ^n term. For this case, the DGF series is one-dimensional, containing the term $\mathcal{R}^0_{k-\frac{1}{2},k-\frac{1}{2}} = 1$ only, hence the computational complexity can be regarded as $\mathcal{O}(1)$ (see Eq. (33)). Define the dimensionality of the Green's vector in Eq. (33) as w, where w is also the dis-

tance of a given spatial point from the edge $k = n$. For such a point, each term in Eq. (33) has a computational complexity that is linear with the order of that term. Summing up all of these terms, the resultant computational complexity for this point becomes $\mathcal{O}(w^2)$.

The total computational region of interest is contained within a spatial window $W = w_{\max}$, defined, say, by the given pulse. The ultimate computational cost is therefore $\mathcal{O}(W^3)$. This value may be compared with the computational cost of the conventional FDTD, that is $\mathcal{O}(kn)$. Obviously, the present method will have the advantage for relatively small values of W, in particular for pulses that have traversed long spatial distances, i.e., where the total computational region is large. In cases where the observation point is far from the characteristic, a straightforward FDTD computation may serve the purpose better, as has been done in [12–14]. In the latter cases, the GDF was computed over the boundary of the computational domain only, to account for possible reflections from the external domain. Obviously, if the external domain is free space, then only numerical dispersion artifacts are responsible for such reflections, since the center of the pulse has long propagated beyond the boundary, i.e., the observation coordinates are as far from the characteristic as can be. It should, however, be noted that for cases like this, the FDTD can be replaced by the recursive formulas such as (10) and (14) and (17). While being of the same complexity as the FDTD, these formulas provide a desirable γ-independent solution.

4. Incorporation of arbitrary boundary conditions

The foregoing discussion has been related to the free space case, where all causal paths are counted. Truncation of the spatial domain by boundaries such that the vertical line in Fig. 16 should be considered in cases when (a) a certain boundary condition is imposed in the vicinity of the boundary, or (b) when the computational domain is to be characterized as a building block in the context of domain decomposition (diakoptic) construction of the entire space, using its scattering or impedance/admittance parameters. For cases such as these, a revised formulation is needed, where interaction with the points beyond the boundary is left to the additional boundary condition, i.e., paths that pass through these points are not counted. In this way, one can accommodate the option of other boundary conditions in the form of additional relationships between field points at the vicinity of the boundary. In the absence of such relationships, the straightforward omission of these paths, or the annulment of the fields beyond the boundary translates into hard boundaries such as PEC or PMC.

In order to evaluate the field at the point of interest at $(n,k) = (N,Z)$ (the encircled point in Fig. 16), one needs first to find the free space PCVs $\mathcal{R}$ or $\mathcal{P}$ given by Eqs. (12) and (16) for the aperture and dual region problems, respectively. The foregoing formulations for both problems are identical, therefore we define $\mathcal{Q} = \mathcal{P}$or $\mathcal{R}$. One is then required to subtract all PCV elements leading from the points $(n, Z + \frac{1}{2})$, adjacent

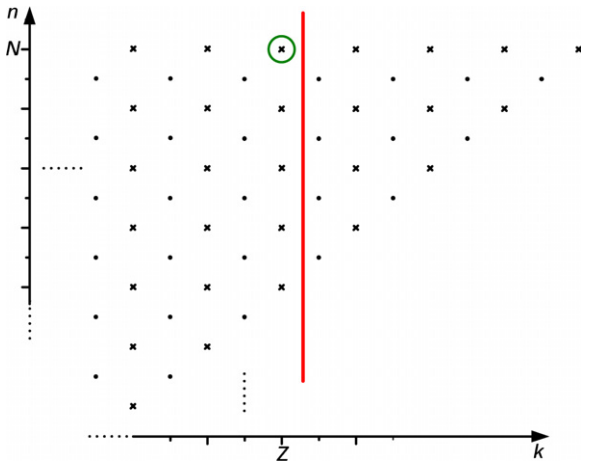

Fig. 16. The modified triangle in the time-space region.

to the right hand side of the red line in Fig. 16, to (N,Z) from $\mathcal{Q}$. For each of these points, the PCV elements to be subtracted are the products of (a) the path counts $\mathcal{Q}^i_{n,Z+\frac{1}{2}}$, where $Z+\frac{1}{2}<n<N-\frac{1}{2}$, and (b) the PCV elements between these points and (N,Z), i.e., the MCNs $\mathcal{R}^i_{N-n,\frac{1}{2}}$. The summation of all these products is now subtracted from $\mathcal{Q}$, leading to the net path count $\widetilde{\mathcal{Q}}$. Starting with $i=0$, we have

$$\widetilde{\mathcal{Q}}_{N,Z}=\mathcal{Q}_{N,Z}-\left\{\mathcal{Q}_{N-\frac{1}{2},Z+\frac{1}{2}}\cdot\mathcal{R}_{\left[\left(Z+\frac{1}{2}\right)-\left(Z+\frac{1}{2}\right)\right],0}+\mathcal{Q}_{N-\frac{3}{2},Z+\frac{1}{2}}\cdot\mathcal{R}_{\left[\left(Z+\frac{3}{2}\right)-\left(Z+\frac{1}{2}\right)\right],0}+\cdots+\mathcal{Q}_{Z+\frac{3}{2},Z+\frac{1}{2}}\cdot\mathcal{R}_{\left[\left(N-\frac{3}{2}\right)-\left(Z+\frac{1}{2}\right)\right],0}\right.$$
$$\left.+\mathcal{Q}_{Z+\frac{1}{2},Z+\frac{1}{2}}\cdot\mathcal{R}_{\left[\left(N-\frac{1}{2}\right)-\left(Z+\frac{1}{2}\right)\right],0}\right\}=\mathcal{Q}_{N,Z}-\sum_{h=Z+\frac{1}{2}}^{N-\frac{1}{2}}\left\{\mathcal{Q}_{[(N+Z)-h],Z+\frac{1}{2}}\cdot\mathcal{R}_{\left[h-\left(Z+\frac{1}{2}\right)\right],0}\right\}. \tag{39}$$

For arbitrary values of i, the following equation holds:

$$\widetilde{\mathcal{Q}}^i_{N,Z}=\mathcal{Q}^i_{N,Z}-\sum_{h=Z+\frac{1}{2}}^{N-\frac{1}{2}}\sum_{s=0}^{i}\left\{\mathcal{Q}^{i-s}_{[(N+Z)-h],Z+\frac{1}{2}}\cdot\mathcal{R}^{,0s}_{\left[h-\left(Z+\frac{1}{2}\right)\right]}\right\}. \tag{40}$$

5. Numerical simulations: one-dimensional pulse propagation

As an example for the aperture problem, we choose the following pulse as describing the electric field at $z=0$ (see Fig. 17(a)):

$$P(n)=\begin{cases}\sin^{\alpha}\left(\frac{\pi}{N}n\right), & 0\leqslant n\leqslant N\\ 0, & \text{elsewhere}\end{cases} \tag{41}$$

with $\alpha=2$. The pulse is sampled at the rate of $M=10$ samples per wavelength and propagated using the DGF as developed for the aperture problem in Section 3 and compared with a conventional FDTD run. The spectral content of the pulse is shown in Fig. 17b for three values of α, although the example below pertain to $\alpha=2$ only as shown in the green curve in the figure. The frequency is normalized as $\Omega=\omega\Delta t$. One can compare this spectral content to the FDTD pass-band (termed "real numerical wavenumber regime" in [2]), bounded by $\Omega_{\text{cutoff}}=\pi$,1.846, 1.287, 0.82 and 0.403 for $\gamma=1$, 0.8, 0.6, 0.4 and 0.2, respectively. The main lobe and first sidelobe of the spectrum are supported by the pass-band for $\gamma\geqslant 0.6$. For $\gamma=0.4$, only the main lobe is within the pass-band. This low pass smoothing effect thus becomes more visible as the value of γ decreases.

The comparison for the two methods is shown in Fig. 18 in the form of snapshots taken at $t=\tau\Delta t=\tau\gamma\frac{\lambda}{10c}$, where τ is the number of timesteps, such that $t=\frac{6\lambda}{c}$ for all values of γ. The FDTD and DGF solutions

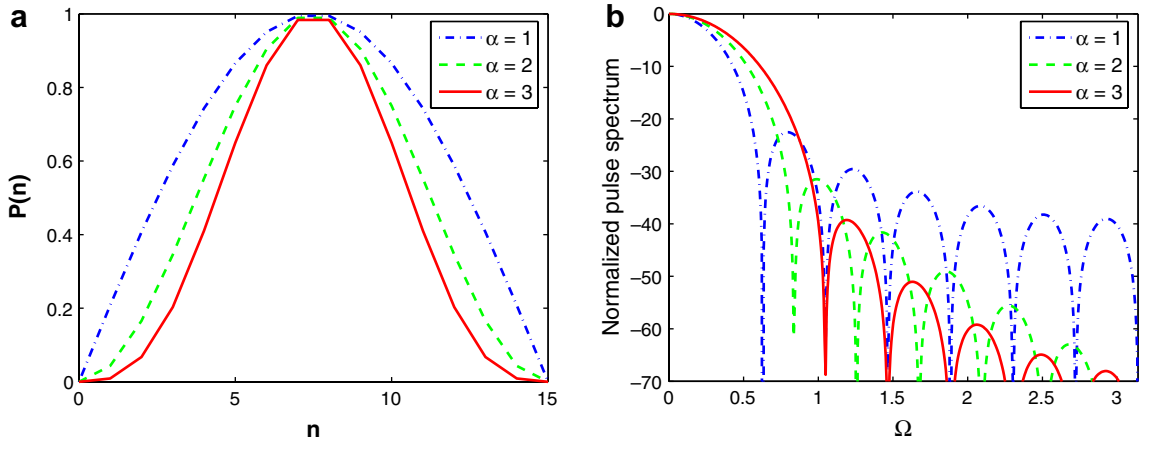

Fig. 17. $P(n)=\sin^{\alpha}\left(\frac{\pi}{N}n\right), 0\leqslant n\leqslant N$ pulse shapes, $\alpha=1$, 2, 3 for dashed-dotted, dotted and solid lines, respectively. (a) Pulse shapes and (b) spectra vs. $\Omega=\omega\Delta t$.

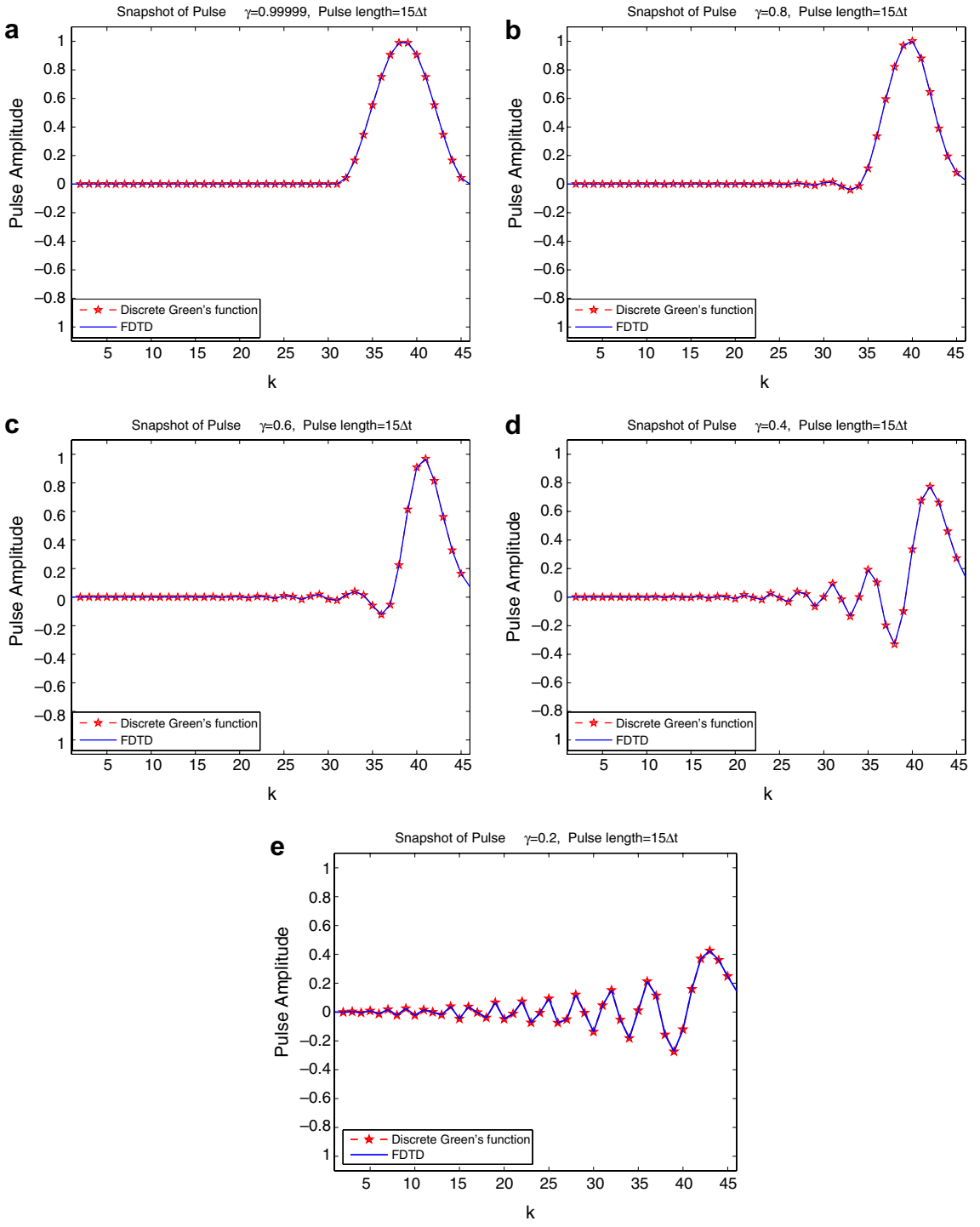

Fig. 18. Pulse propagation for the aperture problem after 45 timesteps using conventional FDTD (solid blue lines) and the Discrete Green's function of Section 3 (dashed lines emphasized with stars) for $\gamma = 0.99999$, 0.8, 0.6, 0.4 and 0.2, ((a)–(e), respectively). (For interpretation of the references in colour in this figure legend, the reader is referred to the web version of this article.)

virtually overlap, as expected. A typical difference between the two curves is of the order of 10^{-14}, depending on the computer precision. This limited time span is used as an example for the computation over the entire domain, as must be done in the context of the conventional FDTD. For longer time spans, the evaluation can be

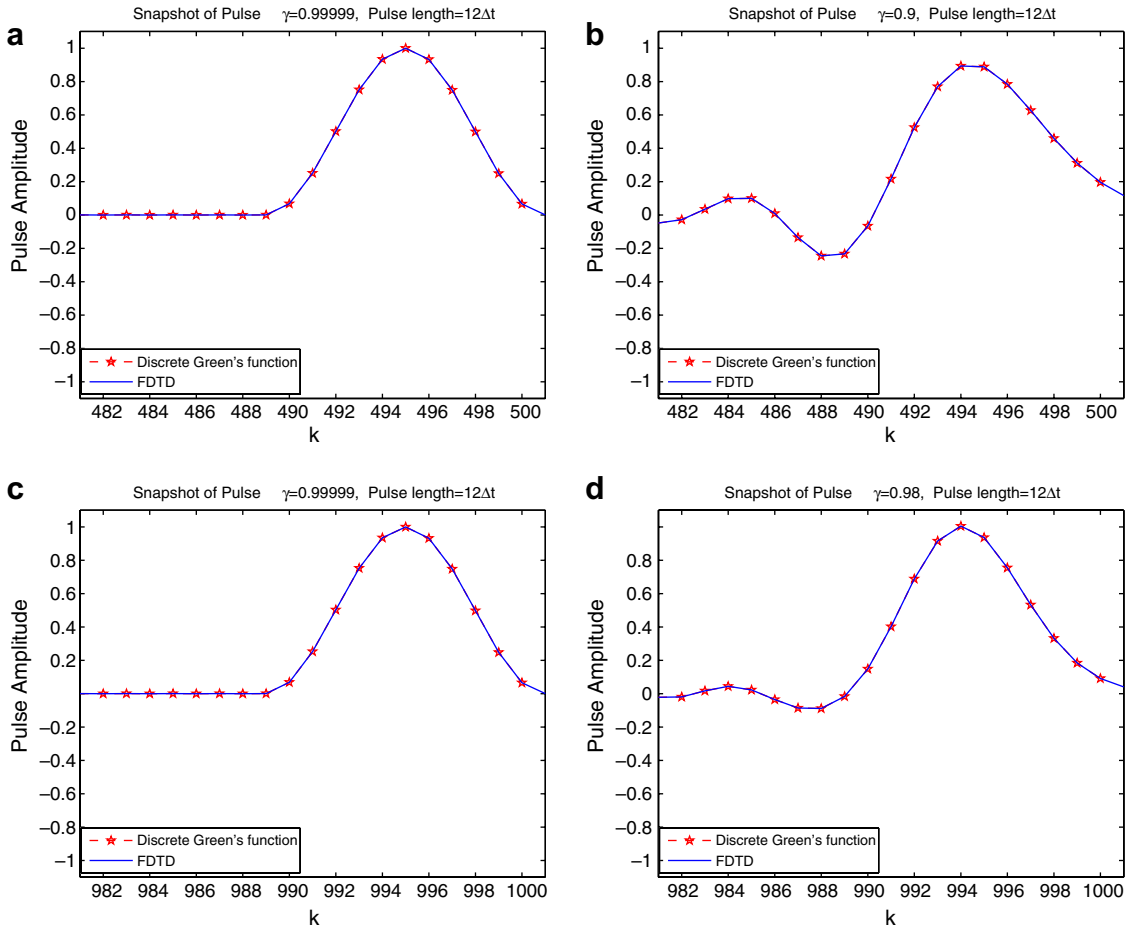

Fig. 19. Pulse propagation for the aperture problem after 500 (a)–(b) and for 1000 (c)–(d) timesteps using conventional FDTD (solid blue lines) and the Discrete Green's function of Section 3 (dashed lines emphasized with stars) for $\gamma = 0.99999$, 0.9, 0.99999 and 0.98, ((a)–(d), respectively). (For interpretation of the references in colour in this figure legend, the reader is referred to the web version of this article.)

restricted to a spatial window around the active region of the pulse, thereby avoiding the need to provide field values throughout the entire computational domain. A snapshot of the pulse at $t = \frac{50\lambda}{c}$ and at $t = \frac{100\lambda}{c}$ within a limited spatial window is shown in Fig. 19, for the different values of γ. The FDTD results have been obtained in the conventional manner over the entire spatial region.

6. Conclusions

The discrete time domain Green's function has been derived in this work from the first principles of the discretized Maxwell's equations in the context of the Yee grid. Analytical expressions for the one-dimensional case have been derived in full and their merits demonstrated numerically by duplicating results obtained via conventional FDTD computations. The two- and three-dimensional cases still needs to be demonstrated. It is conceivable that hybrid numerical and analytical procedures will be formulated for the multi-dimensional and more complex cases. These results can find many applications, including hybridization of differential and integral discrete formulation for absorbing boundary conditions and diakoptic construction of the computational domain, and for bridging the gap over large regions of white spaces in multi-object scattering problem, to name but a few.

References

[1] K.S. Yee, Numerical solution of initial boundary value problems involving Maxwell's equations in isotropic media, IEEE Trans. Antennas and Propagation 14 (3) (1966) 302–307.
[2] A. Taflove, S.C. Hagness, Computational-electrodynamics: The Finite-difference Time-domain Method, second ed., Artech House, Boston, 2000.
[4] D. Jiao, M. Lu, E. Michielssen, J.-M. Jin, A fast time-domain finite element – boundary integral method for electromagnetic analysis, IEEE Trans. Antennas Propagat 49 (10) (2001) 1453–1461.
[5] A. Boag, A. Boag, R. Mittra, A numerical absorbing boundary condition for edge-based finite element analysis, Microwave Opt. Technol. Lett. 7 (16) (1994) 733–737.
[6] A. Boag, U. Shemer, R. Kastner, Hybrid absorbing boundary conditions based on fast non-uniform grid integration for non-convex scatterers, Microwave Opt. Technol. Lett. 43 (2) (2004) 102–106.
[7] A. Boag, U. Shemer, R. Kastner, Non-uniform grid accelerated global boundary condition for acoustic scattering, Comput. Methods Appl. Mech. Engg. 195 (2006) 3608–3621.
[8] A.V. Oppenheim, R.W. Schafer, Digital Signal Processing, Prentice-Hall International, London, 1975.
[9] R. Kastner, A multi-dimensional $\mathcal{Z}$-transform evaluation of the discrete finite difference time domain Green's function, IEEE Trans. Antennas Propagat. 54 (4) (2006) 1215–1222.
[10] D.M. Sullivan, Z transform theory and the FDTD method, IEEE Trans. Antennas Propagat. 44 (1) (1996) 28–34.
[11] J. Vazquez, C.G. Parini, Discrete Green's function formulation of FDTD method for electromagnetic modeling, Electron. Lett. 35 (7) (1999) 554–555.
[12] R. Holtzman, R. Kastner, On the time domain discrete Green's function at the FDTD grid boundary, IEEE Trans. Antennas Propagat. 49 (7) (2001) 1079–1093.
[13] R. Holtzman, R. Kastner, E. Heyman, R.W. Ziolkowski, Stability analysis of the Green's function method (GFM) used as an ABC for arbitrarily-shaped boundaries, IEEE Trans. Antennas Propagat. 50 (2002) 1017–1029.
[14] R. Holtzman, R. Kastner, E. Heyman, R.W. Ziolkowski, Ultra wide band cylindrical antenna design using the Green's function method (GFM) as an absorbing boundary condition (ABC) and radiated field propagator in a genetic optimization approach, Microwave Opt. Technol. Lett. 48 (2) (2006).
[15] Eric W. Weisstein, "Catalan's Triangle" From MathWorld-A Wolfram Web Resource. http://mathworld.wolfram.com/CatalansTriangle.html.
[16] L.B. Felsen, N. Marcuvitz, Radiation and Scattering of Waves, Prentice-Hall, Englewood Cliffs, NJ, 1973.